Appl. Phys. B 62, 345–356 (1996)

Applied Physics B Lasers and Optics

Spectroscopic and fluorescence properties of erbium pentaphosphate (ErP_5O_{14}) monocrystals

F. Kaczmarek, A. Jendrzejczak

Quantum Electronics Laboratory, Institute of Physics, A. Mickiewicz University, PL-60-780 Poznań, Poland
(Fax: +48-61/658962 E-mail: EFKA @ plpuam 11.amu.edu.pl)

Received: 12 May 1995/Accepted: 5 October 1995

Abstract. Erbium pentaphosphate monocrystals (ErP_5O_{14}) were grown and their spectroscopic and fluorescence properties were determined. Also infrared-to-visible up-conversion was observed.

PACS: 42.65.Ky; 42.70.Hj

Erbium-doped crystals and glasses, and especially erbium-doped optical fibers play an essential role in amplification and generation of light in the infrared region [1–6]. Also infrared-to-visible up-conversion appears to be quite efficient in these media [7–16]. The aim of this work was to grow erbium pentaphosphate monocrystals and to determine their spectroscopic and fluorescence properties. Rare-earth pentaphosphates are well-known as "pure" or stoichiometric laser active materials [17–24]. Active ion concentration in these media is of the order of 10^{22} cm^{-3}, however, due to their specific ribbon-like crystal structure, quenching of fluorescence is not so strong as one could expect.

Crystallographic structure of ErP_5O_{14} was determined as a monoclinic one by Jeżowska-Trzebiatowska et al. [25]. Crystal growth and also crystallographic X-ray investigations of monoclinic and orthorhombic polymorphs of ErP_5O_{14} were described by Kaczmarek et al. in two separate papers [26, 27]. Samples of the monoclinic or orthorhombic forms can be difficult to distinguish. Despite their much different structures the unit cell dimensions of the two forms are similar. We have found that monoclinic or orthorhombic polymorphs were obtained in different growing cycles. In the monoclinic form there are two crystallographically different Er^{3+} ions which lie on a twofold axis. The coordination of both cations by 0-atoms is eightfold and may be described as a square antiprism. Precise Raman investigations combined with X-ray measurements revealed that Raman spectra yielded a very simple method for determination of the specific kind of polymorph. We have also found that the efficiency of infrared-to-visible up-conversion is by about an order of magnitude higher in the monoclinic polymorph (relative to the orthorhombic one). Our further measurements were mostly performed on the monoclinic ErP_5O_{14} crystals. Details on the crystal structure of both polymorphs are given in [25–27], however, to illustrate the non-equivalent positions of Er^{3+} in the monoclinic form, a simplified model of the unit cell is shown in Fig. 1. Er(1) and Er(2) ions form zigzag chains along the crystallographic *c*-axis, with Er(1)–Er(1), and Er(2)–Er(2) distances of 6.24 and 6.21 Å, respectively. Both Er(1) and Er(2) ions form further zigzag chains along the *a*-axis with Er(1)–Er(2) distances of 6.45 Å. In addition, the Er(1) and Er(2) ions form linear chains along the *b*-axis with alternating distances of 5.70 and 7.02 Å. In the orthorhombic form, the positions of different Er^{3+} ions in the crystal structure are equivalent. Another way to recognize the kind of polymorph is to find the cleavage plane. The orthorhombic crystals exhibit a perfect cleavage plane perpendicular to *z*; there are no cleavage planes in the monoclinic samples.

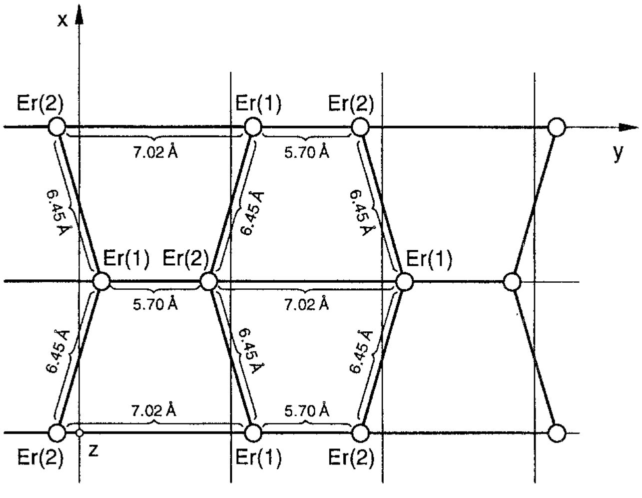

Fig. 1. A simplified display of Er^{3+} ions within the unit cell of monoclinic symmetry

Table 1. A short characteristics of the ErP_5O_{14} sample used

No. of sample	Crystallographic structure	Thickness [mm]	Length or diameter [mm]	Macroscopic morphology
1	Monoclinic	0.71	4	Hexagonal
4	Monoclinic	0.15	3	Hexagonal
9	Monoclinic	0.61	5	Hexagonal
12	Monoclinic	1.5	5	Undetermined
Pr	Monoclinic (powdered sample) ErP_5O_{14}:KBr = 1:100	—	—	—
7	Orthorhombic	1.5	7	Hexagonal
11	Orthorhombic	1.0	6	Hexagonal

1 A short description of the samples

Concentration of Er^{3+} ions in an ErP_5O_{14} monocrystal amounts to 3.78×10^{21} cm^{-3}. The measured density, ρ, is 3.64 g/cm^3, and the refractive index (along the z-axis) – 1.71 (at $\lambda = 632.8$ nm). Table 1 specifies the parameters of the samples used in our investigations. Tens of other samples were also checked for comparison.

2 Measurements of absorption (or absorbance)

2.1 Room temperature

Measurements of absorption coefficient, α, or absorbance, A, were performed in wave number band from 6000 cm^{-1} up to 43749 cm^{-1}, using a Varian spectrophotometer. A simplified display of absorbance is shown in Fig. 2a. To excite erbium-doped laser media, and also when studying infrared-to-visible up-conversion, laser diodes emitting at 800 nm or 970 nm are most frequently used. Absorption bands at these wavelengths measured for ErP_5O_{14} monocrystal at room temperature are shown in Fig. 2b.

As seen, $\alpha(970\text{ nm})/\alpha(800\text{ nm}) \cong 3.16$. The main fluorescence band at about 1.53 μm is also characterized by strong absorption. Using formula (1) and measuring the area under the absorption bands, we calculated the overall oscillator strengths for absorption at 800 and 970 nm: $f(\lambda = 800\text{ nm}) = 40 \times 10^{-8}$, and $f(\lambda = 970\text{ nm}) = 194 \times 10^{-8}$. In the course of the absorption, Raman and infrared measurements, the probe beam was sent in the z-direction, i.e. perpendicularly to the largest surface. The light was not polarized. Additionally, two kinds of Raman spectra were taken for a polarized beam. The results are given below. In calculations of the oscillator strengths we have used the following formula:

$$f = \frac{mc}{\pi N e^2}\chi \int \alpha(\tilde{\nu})\,d\nu = \frac{mc^2}{\pi N e^2}\int \alpha(\tilde{\nu})\,d\tilde{\nu}, \qquad (1)$$

where α and ν are expressed in cm^{-1}, $e = 4.803 \times 10^{10}$ esu, $m = 9.108 \times 10^{-28}$ g, $N = 3.78 \times 10^{21}$ cm^{-3} and $\chi = 9n/(n^2 + 2)^2$ is a correction factor depending on the refractive index of the medium ($n = 1.71$ in our case).

The overlapping of many individual lines does not permit a straightforward calculation of the integral $\int \alpha(\nu)\,d\nu$. For this reason, we have written a computer program to

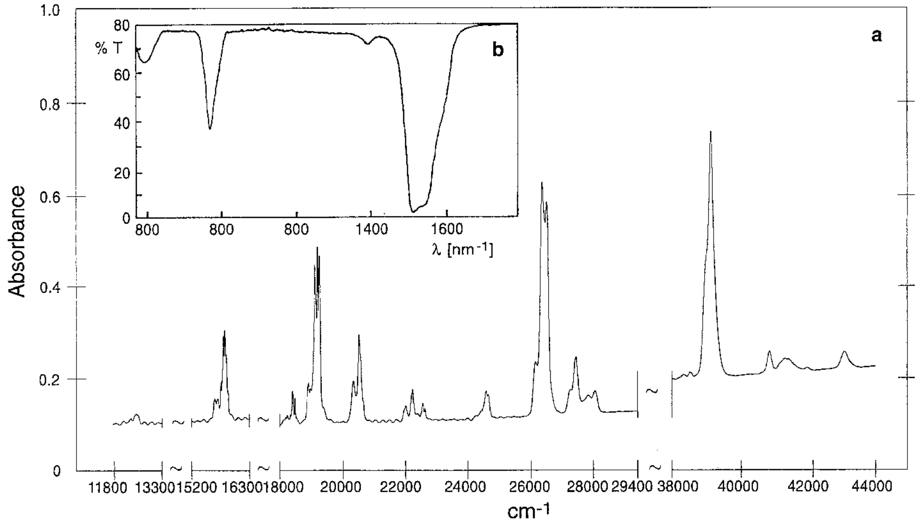

Fig. 2a, b. Absorbance of ErP_5O_{14} monocrystal measured at room temperature sample no. 1 (**a**). Absorption at the main laser diode pumping bands (**b**)

Table 2. LSJ designation, center wave number, ν [cm^{-1}], peak absorption coefficient, α_p[cm^{-1}], FWHM, $\Delta\nu$ [cm^{-1}], oscillator strengths, f, for the $^4I_{15/2} \rightarrow$ up transitions in ErP_5O_{14} monocrystal at room temperature. Sample no. 1

LSJ designation	Center wave number ν [cm^{-1}]	α_{peak} [cm^{-1}]	FWHM $\Delta\nu$ [cm^{-1}]	$f \times 10^8$
$^2I_{13/2}$	43 749	0.90	111	4.10
	43 513	5.42	123	27.11
	43 217	0.22	80	0.71
$^4D_{3/2}$	42 312	1.04	85	3.58
$^2D_{3/2}$	41 942	1.49	181	10.97
	41 744	3.19	116	15.03
	41 584	2.29	91	8.45
$^2L_{17/2}$	41 444	2.55	142	14.66
	41 232	0.59	46	1.11
	41 112	7.29	76	22.39
$^2I_{11/2}$	40 947	0.74	105	3.15
$^4D_{7/2}$	39 628	2.16	103	9.03
	39 355	26.92	125	137.72
	39 237	62.75	71	181.27
	39 074	37.28	93	140.22
	38 831	1.72	103	7.17
	38 589	2.63	71	7.63
$^4D_{5/2}$	38 378	1.93	82	6.44
$^2G_{7/2}$	28 080	6.55	82	21.82
	27 852	6.32	145	37.46
$^2K_{15/2}$	27 629	3.07	91	11.33
	27 446	19.11	79	61.08
$^2G_{9/2}$	27 252	8.23	86	28.64
$^4G_{11/2}$	26 636	7.7	123	38.55
	26 511	64.15	64	167.39
	26 365	76.03	71	218.97
	26 156	18.09	87	64.05
$^2H_{9/2}$	24 743	0.88	77	2.76
	24 660	7.24	40	11.86
	24 581	8.37	38	12.96
	24 518	2.98	34	4.16
	24 431	2.91	84	9.91
	24 240	1.33	59	3.21
$^4F_{3/2}$	22 696	0.91	59	2.20
	22 630	3.79	19	3.00
	22 566	3.84	27	4.29
	22 533	2.82	49	5.69
$^4F_{5/2}$	22 394	2.59	57	6.02
	22 317	1.55	31	1.96
	22 276	4.86	20	3.93
	22 229	8.43	24	8.31
	22 186	7.10	33	9.50
	22 110	1.58	41	2.65
	22 014	5.28	45	9.55
	21 940	2.67	34	3.73
$^4F_{7/2}$	20 841	0.55	51	1.15
	20 733	1.00	44	1.77
	20 657	6.65	28	7.74
	20 612	8.56	20	6.93
	20 574	15.43	22	13.80
	20 516	28.83	36	41.88
	20 438	5.83	41	9.63
	20 333	13.63	64	35.61
$^2H_{11/2}$	19 419	4.28	51	8.93
	19 311	7.50	50	15.33
	19 249	54.34	30	65.92
	19 189	54.48	19	42.31
	19 147	32.98	17	23.63
	19 106	47.30	23	43.92
	19 059	18.16	33	24.37

Table 2 (Continued)

LSJ designation	Center wave number ν [cm^{-1}]	α_{peak} [cm^{-1}]	FWHM $\Delta\nu$ [cm^{-1}]	$f \times 10^8$
$^4S_{3/2}$	18 976	11.46	42	19.59
	18 898	10.96	33	14.68
	18 845	2.96	53	6.32
	18 562	1.23	38	1.89
	18 508	1.93	31	2.43
	18 480	7.48	12	3.72
	18 424	6.30	27	6.85
	18 401	6.48	21	5.45
	18 345	3.15	27	3.51
	18 291	1.21	23	1.17
	18 234	3.03	34	4.14
	18 180	1.76	19	1.34
	18 124	1.94	24	2.80
$^4F_{9/2}$	15 987	0.79	72	2.31
	15 773	0.97	56	2.19
	15 523	2.12	80	6.81
	15 439	8.51	23	7.94
	15 384	20.75	24	20.13
	15 335	29.00	22	25.97
	15 294	23.40	14	13.69
	15 260	16.00	20	12.95
	15 218	11.66	15	6.96
	15 122	7.29	46	13.52
	15 020	7.40	44	13.38
	14 891	1.07	50	2.14
	14 661	0.91	52	1.93
$^4I_{9/2}$	12 572	2.58	43	4.45
	12 492	3.31	46	6.19
	12 430	1.18	25	1.19
	12 330	2.15	60	5.21
	12 102	1.33	43	2.33
$^4I_{15/2}$	352		Ground state	
	302			
	256			
	146			
	88			
	72			
	58			
	0			

select each individual line, and then the line shape has been fit to a Gaussian profile: Lorentz line fitting was less accurate. So, we have

$$\alpha(\nu, \nu_0) = G(\nu, \nu_0)\alpha_{\mathrm{int}}; \quad \alpha_{\mathrm{int}} = \int \alpha(\nu)\,\mathrm{d}\nu,$$

$$G(\nu, \nu_0) = \frac{1}{\sqrt{2\pi}\sigma} \exp\left(-\frac{(\nu - \nu_0)^2}{2\sigma^2}\right); \quad \sigma = \frac{\Delta\nu}{\sqrt{2\ln 2}}$$

is the normalized Gaussian line, and

$$\int \alpha(\nu, \nu_0)\,\mathrm{d}\nu = \alpha_{\mathrm{int}} \int G(\nu, \nu_0)\,\mathrm{d}\nu = \alpha_{\mathrm{int}},$$

since

$$\int G(\nu, \nu_0)\,\mathrm{d}\nu = 1.$$

In this way, we obtain

$$\alpha(\nu = \nu_0) = \alpha_{\mathrm{peak}} = G(\nu = \nu_0)\alpha_{\mathrm{int}}.$$

Hence,

$$\alpha_{\mathrm{int}} = \frac{\alpha_{\mathrm{peak}}}{G(\nu = \nu_0)} = \frac{\alpha_{\mathrm{peak}}\sqrt{\pi}\Delta\nu}{\sqrt{\ln 2}} = 2.13 \cdot \Delta\nu \cdot \alpha_{\mathrm{peak}},$$

where $\Delta\nu$ is the full width at half maximum (FWHM). And finally (for the ErP_5O_{14} monocrystal) and for $\Delta\nu$ expressed in cm^{-1}:

$$f = 0.408 \times 10^{-9} \cdot \alpha_{\mathrm{peak}} \cdot \Delta\nu.$$

Table 2 summarizes the results of our measurements and calculations.

Column no. 1 of this table presents LSJ labelling that was estimated after Donlan and Santiago [28], Mazurak et al. [29], Li et al. [30], Krupke [31, 32], Carnall [33], Rajniak [34] and Weber [35]. Measurements at room temperature are essential for practical applications. The LSJ labelling in column no. 1 must be considered as an experimental assignment for the absorption lines found.

2.2 Low-temperature measurements at 5 K

To obtain a highly resolved absorption spectrum, the ErP_5O_{14} monocrystals (of monoclinic symmetry) were cooled down to 5 K. This temperature ensures high population of the lowest level of the ground state manifold, leaving all the other sublevels empty. In this way, the initial level (for absorption) was well-determined. Figure 3 illustrates absorbance in the wave number band from 6900 to 27 000 cm^{-1}. The main pumping band at about 12 500 cm^{-1}, hardly seen at room temperature, has been very well resolved at 5 K.

Table 3 presents wave numbers and peak absorption coefficients for the absorption lines measured.

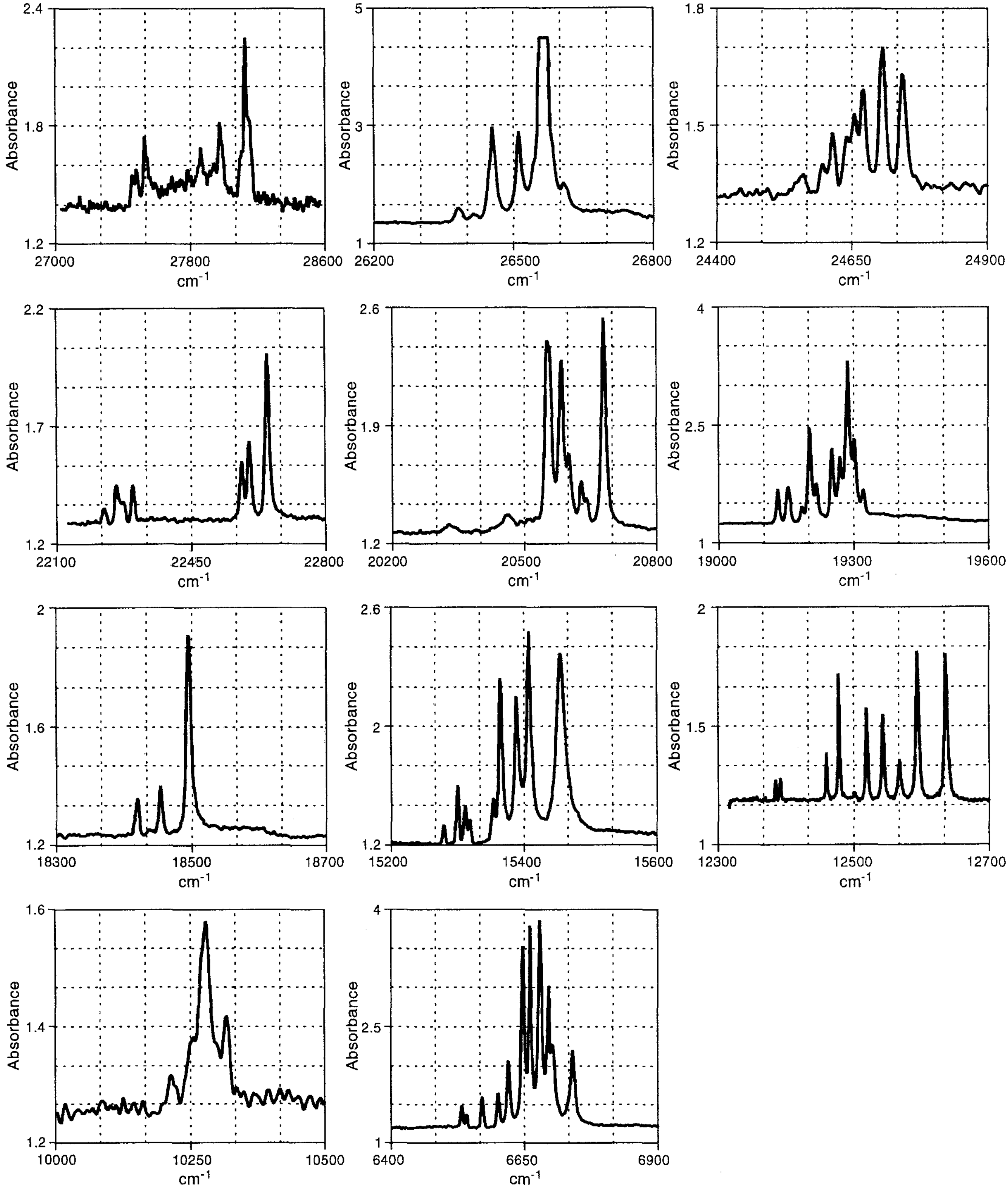

Fig. 3. Absorption spectrum of ErP_5O_{14} monocrystal measured at 5 K. Sample no. 1

Table 3. LSJ designation of the transition involved, center wave number, ν [cm^{-1}], and peak absorption coefficient, α [cm^{-1}] of ErP_5O_{14} monocrystal at 5 K, measured in the wavelength band from 1530 to 355 nm. Sample o. 1

LSJ designation	Center wave number ν [cm^{-1}]	Peak absorption coefficient α [cm^{-1}]
$^4I_{13/2}$	6532	8.92
	6541	5.43
	6570	12.56
	6600	14.14
	6620	27.63
	6647	75.13
	6660	83.83
	6678	86.02
	6695	58.53
	6702	34.22
	6740	31.88
$^4I_{11/2}$	10 214	1.90
	10 256	3.96
	10 278	10.37
	10 316	5.06
$^4I_{9/2}$	12 384	3.44
	12 391	3.79
	12 459	7.78
	12 477	20.31
	12 518	15.15
	12 542	13.72
	12 567	6.48
	12 593	23.94
	12 635	23.07
$^4F_{9/2}$	15 278	3.01
	15 299	11.53
	15 311	7.01
	15 317	3.92
	15 352	8.44
	15 365	34.66
	15 388	30.62
	15 407	44.67
	15 455	39.86
$^4S_{3/2}$	18 419	3.85
	18 453	5.20
	18 494	21.68
$^2H_{13/2}$	19 131	14.18
	19 153	14.98
	19 184	6.73
	19 201	39.73
	19 216	16.54
	19 252	31.13
	19 270	27.78
	19 287	66.82
	19 301	34.98
	19 320	13.90
$^4F_{7/2}$	20 550	36.69
	20 584	32.98
	20 601	15.09
	20 628	9.67
	20 639	6.50
	20 679	41.08
$^4F_{5/2}$	22 223	2.01
	22 255	5.24
	22 271	2.89
	22 296	5.23
$^2F_{3/2}$	22 581	8.12
	22 601	10.86
	22 648	22.7
$^2H_{9/2}$	24 559	1.62
	24 596	2.41
	24 612	4.89
	24 639	4.60
	24 654	6.48
	24 671	8.40
	24 706	12.02
	24 742	9.70
$^4G_{11/2}$	26 378	7.93
	26 415	4.04
	26 454	51.58
	26 511	49.18
	26 563	101.19
	26 606	21.39
$^2G_{9/2}$	27 452	5.41
	27 478	6.35
	27 526	11.60
$^2G_{7/2}$	27 857	9.74
	27 972	13.81
	28 123	27.75

Careful examination of the fluorescence and absorption lines enabled determination of the ground state manifold, $^4I_{15/2}$ (see Table 2).

3 Raman and infrared spectra

Raman and infrared spectra were taken at room temperature for a few ErP_5O_{14} monocrystals as well as for a powdered sample. A typical Raman spectrum (for sample no. 7, orthorhombic) taken with a Bruker IFS 66 spectrograph is shown in Fig. 4a. Analogous spectra for a monoclinic sample no. 4 is shown in Fig. 4b. Excitation source: Nd:YAG laser operating at a wavelength of 1.064 μm. We have observed small displacements of the strongest Raman lines for different ErP_5O_{14} samples. Infrared spectrum taken with the Perkin-Elmer spectrograph for a powdered sample is shown in Fig. 5. Table 4 describes the positions, relative intensities and absorbances for the Raman and infrared lines recorded. The strongest lines detected in the IR spectrum were as follows: 484, 734, 943, 970, 1008, 1013, 1040, 1284, 1354, 1359 cm^{-1}. It is known [36] that the following bands are responsible for: P–O stretching (1300–1100 cm^{-1}), P–O–H bending (800–900 cm^{-1}). P–O–P stretching (840–930 cm^{-1}), P–O–P in ring system ($\approx$ 750 cm^{-1}) ionic P–O stretching (1000–1100 cm^{-1}), harmonics of P–O–P stretching – 770 cm^{-1} and lower. As seen from the table the very strong 484 cm^{-1} IR line takes approximately half the frequency of the strongest 943 cm^{-1} line. The infrared spectrum of ErP_5O_{14} is very similar to the one observed for NdP_5O_{14} by Tofield et al. [18]. The strongest lines almost coincide in the two spectra. The same is also true for the Raman spectra. As it was also found by Tofield et al. relative intensities of the lines and their positions in the spectrum changed, from sample to

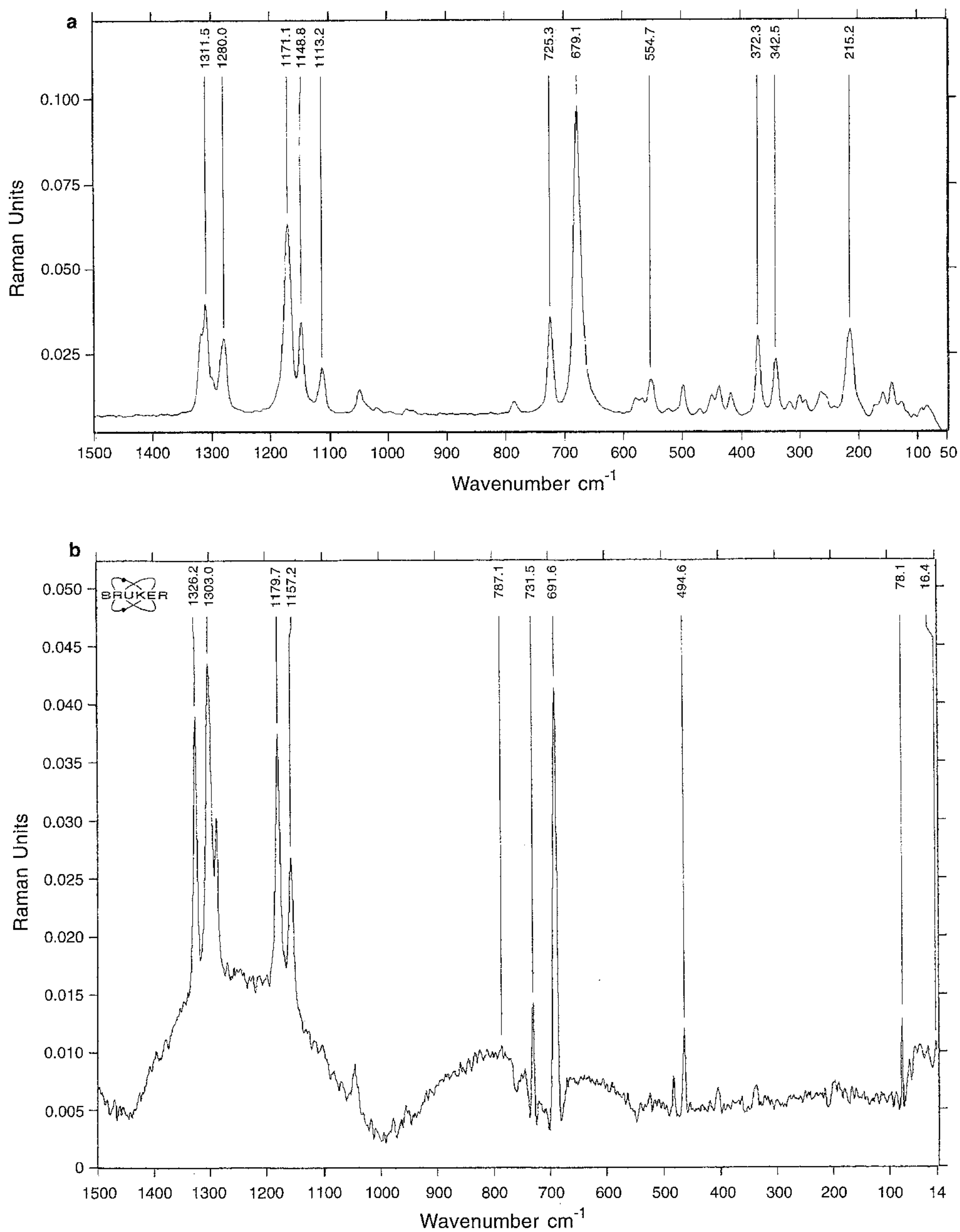

Fig. 4a, b. Raman spectrum of ErP_5O_{14} monocrystal taken at room temperature. **a** Sample no. 7 – orthorhombic; **b** Sample no. 4 – monoclinic

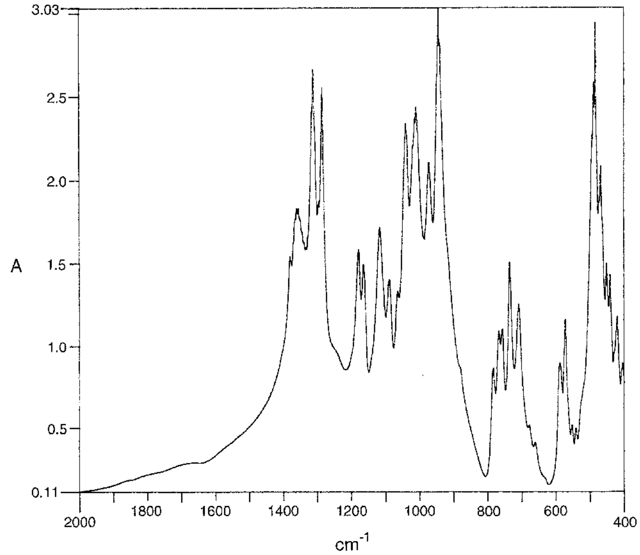

Fig. 5. Infrared spectrum of a powdered ErP_5O_{14} sample (monoclinic)

sample and were strongly affected by crystal inhomogenities. As seen in Table 5, the displacements of the main Raman lines for samples no. 4, 9 and Pr (all of monoclinic symmetry) with respect to samples no. 7 and 11 (both of orthorhombic symmetry) amounts to about 1 cm^{-1}. On the other hand, the difference, $\Delta\nu$, between adjacent Raman lines is larger by about 1 cm^{-1} for samples no. 7 and 11, also relative to samples no. 4, 9 and Pr. This is probably the quickest way, to determine the kind of polymorph, since monoclinic or orthorhombic X-ray investigations are much more troublesome. Depending on the procedure of growth, the optical quality of our crystals differed pronouncedly and it affected not only the IR or Raman spectra but also the efficiency of the up-conversion process studied. Using a polarized incident beam, two

Table 4. Raman lines and their relative intensities of ErP_5O_{14} samples (columns no. 1 and 2). Infrared lines and their absorbances for a powdered ErP_5O_{14} sample are given in columns no. 3 and 4. The Raman spectra were taken for a few ErP_5O_{14} samples, obtained in different growth cycles (numbered in parentheses). For every sample, the intensity of the strongest Raman line was taken as unity. Intensities of the other lines found are compared to this line. Numbers denote monocrystals, Pr - powdered sample

1 $\Delta\nu$ [cm^{-1}]	2 Raman relative intensity	3 $\tilde{\nu}$ [cm^{-1}]	4 Infrared absorbance (powdered sample)
1320.2	0.19 (7)	1315	2.41
1320	≈ 0.15 (7)		
1320.8	0.2 (11)		
1326.2	0.54 (4)		
1325.7	1 (12)		
1325.3	0.58 (Pr)		
—	—	1379	1.54
—	—	1359	1.828
—	—	1354	1.825
1311.8	0.45 (7)	1311	2.665
1311.5	0.45 (7)		
—	—	1294	1.868
1303	0.47 (Pr)	—	—
	0.66 (4)		
	0.53 (11)		
1281.6	0.087 (7)	1284	2.555
1284.7	0.097 (11)		
1287.7	0.18 (Pr)		
1171.3	0.66 (7)	1177	1.581
1171.6	0.68 (11)		
1157	0.3 (4)	1163	1.491
1156	0.36 (12)		
1156	0.27 (Pr)		
1148.8	0.27 (7)	—	—
1148.9	0.32 (11)		
1113.3	0.1 (7)	1116	1.713
	0.14 (11)		
—	—	1088	1.397
—	—	1063	1.327
—	—	1040	2.342
—	—	1013	2.368
—	—	1008	2.437
—	—	970	2.108
—	—	943	3.04
—	—	939	2.823
—	—	782	0.865
—	—	766	1.089
—	—	756	1.101
725.4	0.24 (7)	734	1.504
725.4	0.3 (11)		
731.5	0.27 (4)		
731.0	0.3 (Pr)		
—	—	708	1.247
679.2	1 (7)	678	0.511
679.3	1 (11)		
691.1	1 (4)		
691.4	0.92 (12)		
690.8	1 (Pr)		
—	—	660	0.409
—	—	588	0.896
—	—	572	1.160
554.5	0.170 (7)	552	0.515
554.5	0.078 (11)		
—	—	541	0.496
—	—	494	2.271
499.9	0.064 (11)	489	2.586
484	very weak (7)	484	2.944

Table 4 (Continued)

1 $\Delta\nu$ [cm^{-1}]	2 Raman relative intensity	3 $\tilde{\nu}$ [cm^{-1}]	4 Infrared absorbance (powdered sample)
464.6	0.2 (4)	468	2.086
—	—	451	1.497
438.5	0.064 (11)	441	1.427
—	—	420	1.178
—	—	404	0.892
372.6	0.11 (7)	—	—
372.6	0.16 (11)		
342.7	0.05 (7)	—	—
342.7	0.071 (11)		
293.9	0.46 (12)	—	—
291.6	0.2 (Pr)	—	—
269 (Pr)	0.1 (Pr)	—	—
236.6 (Pr)	0.22	—	—
214.9 (7)	0.25 (7)	—	—
214.8 (11)	0.33 (11)		
144.7 (11)	0.078 (11)	—	—
84.4 (Pr)	0.13 (Pr)	—	—
78.1 (11)	0.2 (11)	—	—

Table 5. Wave numbers and differences between two selected strong adjacent Raman lines found for various ErP_5O_{14} samples

Sample no.	Adjacent line ν_{ad} [cm^{-1}]	Main line ν_m [cm^{-1}]	$\Delta\nu$ [cm^{-1}] $\nu_{ad} - \nu_m$
Monoclinic			
1	729.3	690.8	38.5
4	731.3	690.8	40.5
9	730.7	691.1	39.1
Pr	731.0	690.8	40.2
Orthorhombic			
7	725.3	679.1	46.2
11	725.5	679.3	46.2

kinds of Raman spectra were recorded, with the electric field vector $E \parallel x$, on $E \parallel z$ (see Fig. 6). Almost no differences in the display of Raman lines in the 500–1500 cm^{-1} band were found. In the lower wave number region (0–500 cm^{-1}), the main difference observed was assigned to the lines at 215.3 and 343 cm^{-1}. The first one was very strong for $E \parallel x$ and weak for $E | z$. On the other hand, the 343 cm^{-1} line was weak for $E \parallel x$ and very strong for $E \parallel z$. Results of the Raman studies and their interpretation will be published separately.

According to Miyakawa and Dexter [37] multiphoton relaxation rates become steeply small in the phonon energy region below about 1000 cm^{-1}. Theoretical calculations

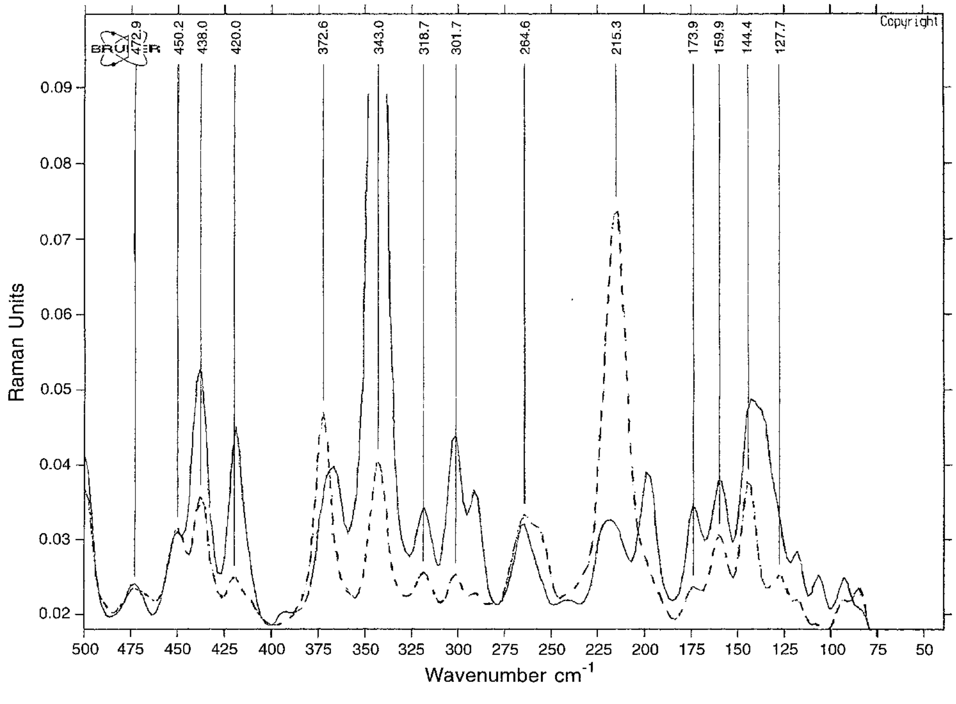

Fig. 6. Raman spectrum of ErP_5O_{14} monocrystal in the 0–500 cm^{-1} band as dependent on the electric field orientation of the incident beam (sample no. 7) recorded at room temperature. $E \parallel z$ (*solid* line), $E \parallel x$ (*dashed line*)

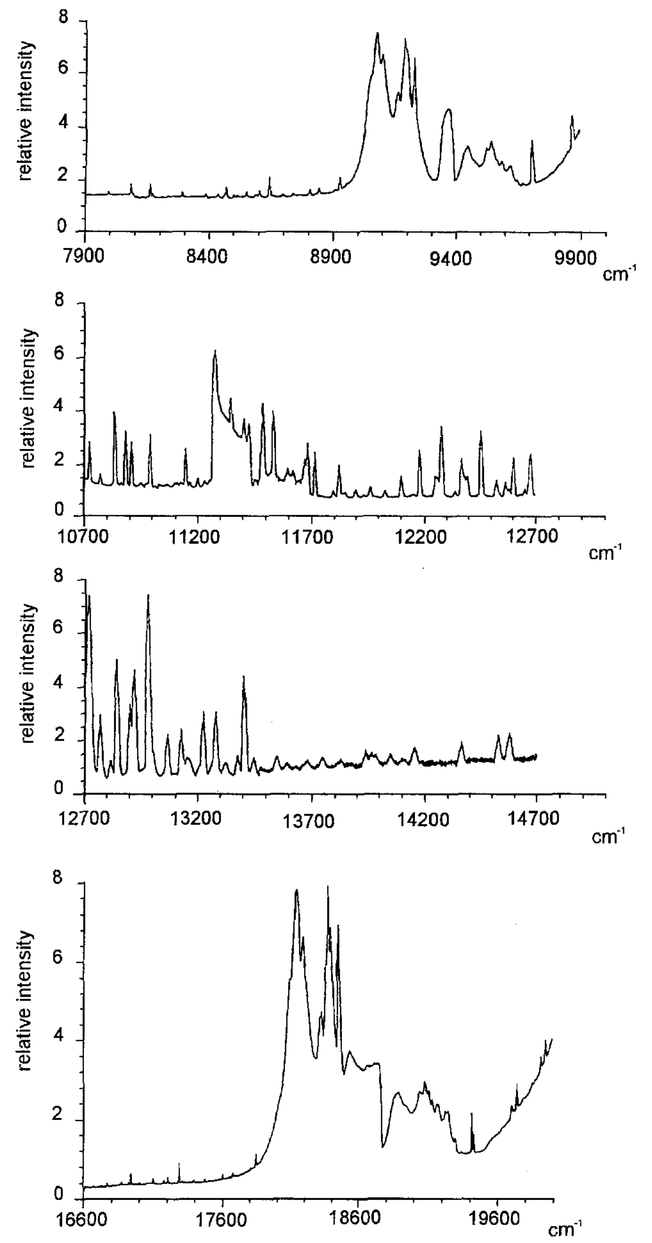

Fig. 7. Fluorescence spectrum of ErP_5O_{14} monocrystal at room temperature

Table 6. Fluorescence lines and their relative intensities of ErP_5O_{14}. Excitation source: ion argon laser, $\lambda = 488$ nm

Wave number of the emission line [cm^{-1}]	LSJ designation upper level	LSJ designation terminal level	Relative intensity
9369	$^2H_{11/2}$	$^4I_{11/2}$	4.04
9379	$^2H_{11/2}$	$^4I_{11/2}$	4.04
10727	$^4I_{11/2}$	$^4I_{15/2}$	2.11
10846	$^4I_{11/2}$	$^4I_{15/2}$	3.13
10893	$^4I_{11/2}$	$^4I_{15/2}$	2.42
10920	$^4I_{11/2}$	$^4I_{15/2}$	2.00
11006	$^4S_{3/2}$	$^4I_{13/2}$	2.00
11309	$^4S_{3/2}$	$^4I_{13/2}$	7.05
11383	$^4S_{3/2}$	$^4I_{13/2}$	3.83
11441	$^4S_{3/2}$	$^4I_{13/2}$	3.07
11461	$^4S_{3/2}$	$^4I_{13/2}$	2.81
11527	$^4S_{3/2}$	$^4I_{13/2}$	2.87
11573	$^4S_{3/2}$	$^4I_{13/2}$	1.96
12225	$^2H_{11/2}$	$^4I_{13/2}$	1.97
12321	$^2H_{11/2}$	$^4I_{13/2}$	2.82
12502	$^2H_{11/2}$	$^4I_{13/2}$	2.56
12724	$^2H_{11/2}$	$^4I_{13/2}$	2.82
12728	$^2H_{11/2}$	$^4I_{13/2}$	2.83
12910	$^2H_{11/2}$	$^4I_{13/2}$	2.56
14810	$^4F_{9/2}$	$^4I_{15/2}$	2.62
14972	$^4F_{9/2}$	$^4I_{15/2}$	5.15
15012	$^4F_{9/2}$	$^4I_{15/2}$	2.75
15065	$^4F_{9/2}$	$^4I_{15/2}$	2.69
15444	$^4F_{9/2}$	$^4I_{15/2}$	2.37
16045	$^4F_{9/2}$	$^4I_{15/2}$	3.34
16231	$^4F_{9/2}$	$^4I_{15/2}$	5.31
18118	$^4S_{3/2}$	$^4I_{15/2}$	8.25
18168	$^4S_{3/2}$	$^4I_{15/2}$	11.59
18214	$^4S_{3/2}$	$^4I_{15/2}$	9.82
18342	$^4S_{3/2}$	$^4I_{15/2}$	6.94
18382	$^4S_{3/2}$	$^4I_{15/2}$	8.86
18398	$^4S_{3/2}$	$^4I_{15/2}$	11.70
18412	$^4S_{3/2}$	$^4I_{15/2}$	10.16
18470	$^4S_{3/2}$	$^4I_{15/2}$	10.25
18898	$^2H_{11/2}$	$^4I_{15/2}$	3.89
19052	$^2H_{11/2}$	$^4I_{15/2}$	3.91
19090	$^2H_{11/2}$	$^4I_{15/2}$	4.28
19114	$^2H_{11/2}$	$^4I_{15/2}$	3.92
19138	$^2H_{11/2}$	$^4I_{15/2}$	3.59
19170	$^2H_{11/2}$	$^4I_{15/2}$	3.42
19182	$^2H_{11/2}$	$^4I_{15/2}$	3.43
19232	$^2H_{11/2}$	$^4I_{15/2}$	3.15
19254	$^2H_{11/2}$	$^4I_{15/2}$	3.15
19420	$^2H_{11/2}$	$^4I_{15/2}$	3.06

made by Weber [35] suggest that the most critical factor affecting the rate of multiphonon relaxation is the energy gap to next-lower level. An empirical formula found for many rare-earth ions states that this multiphonon decay rate exhibits an approximately exponential dependence on the energy gap, ΔE

$$k = W(o)e^{-\alpha\Delta E},$$

where $W(o)$ and α are constants.

As seen in the energy level diagram (Fig. 4), the gap between $^4S_{3/2}$ level and the nearest lower level amounts to $\sim 3100\ cm^{-1}$. Even four-phonon relaxation of the main Raman or infrared lines found does not concide with this energy gap. However, as it was shown by Weber [35], the multiphonon rate, k, for an energy gap of $2950\ cm^{-1}$ between $^4S_{3/2}$ and the lower lying level of Er^{3+} in yttrium orthoaluminate matrix, amounts to 3.6×10^3, which cannot be neglected in the process of fluorescence quenching. Nevertheless, we must conclude that the concentration quenching of the $^4S_{3/2}$ fluorescence level is mainly responsible for the observed low efficiency of the process of infrared-to-visible up-conversion. Lifetime measurements of the $^4S_{3/2}$ state of Er^{3+} in different crystals or glasses revealed [38, 39] that this lifetime is about 150 μs for low Er^{3+} concentration and decreases to about 4 μs for Er^{3+} concentration of $4 \times 10^{21}\ cm^{-3}$. Lifetime measurements of some selected energy levels of Er^{3+} in ErP_5O_{14} monocrystals are under way in our laboratory.

4 Fluorescence spectrum of ErP_5O_{14}

Fluorescence spectrum of a powdered ErP_5O_{14} sample was taken at room temperature using an argon ion laser as an excitation source. The spectrum is shown in Fig. 7. Table 6 presents the numerical results for the fluorescence lines found.

4.1 Fluorescence in the "green" – infrared-to-visible up-conversion (monoclinic samples)

Infrared exciting beam ($\lambda = 800\ \mu m$) has been focused to a diameter of 0.25 mm or 0.4 mm within an ErP_5O_{14} monocrystal, about 1.5 mm in thickness. We have used an SDL-2372-P3 laser diode of Spectra Diode, capable of emitting up to 1.2 W, at a wavelength of about 800 nm. Fluorescence in the green at 543 nm was seen along the exciting beam, and was detected perpendicularly to this beam as a function of the incident infrared power at room temperature, and also, at the liquid nitrogen temperature. Due to intense heating of the monocrystal it was immersed in water, or directly in the liquid nitrogen bath. Fluorescence intensity as a function of the incident power is shown in Fig. 8. The graph clearly indicates the nonlinear dependence, expected for the cooperative process of excitation. Fluorescence intensity increases by a factor of 3.2 when the sample was cooled from room temperature down to the liquid nitrogen temperature. For a typical beam power of 500 mW, the power density within the crystal amounts to 1.0 kW/cm^2. We have also checked the threshold incident power for fluorescence to occur in the green. Although there is no sharp transition between zero fluorescence and the detectable one, the threshold amounts to 16 mW, i.e. to 12 W/cm^2 (calculated for a measured beam waist within the crystal). The green fluorescence path within the crystal was clearly visible at daylight, however, attempts to obtain laser emission at that wavelength for CW excitation at room temperature, and also at liquid nitrogen temperature failed. Infrared-to-visible up-conversion in orthorhombic samples was by about an order of magnitude weaker.

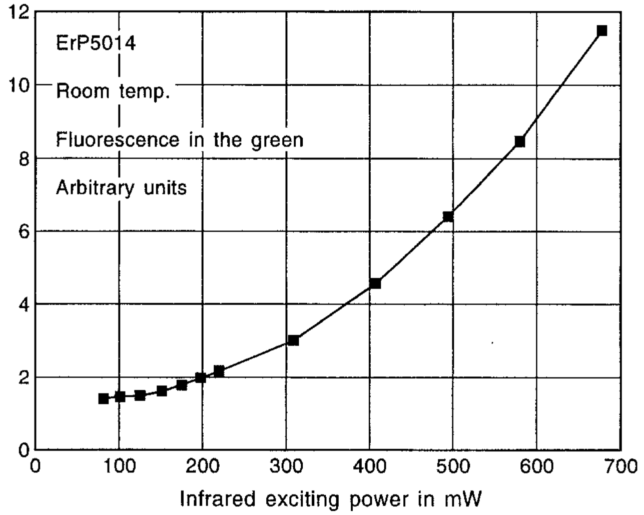

Fig. 8. Infrared-to-visible up-conversion as function of the power of the infrared beam ($\lambda = 800$ nm)

5. Conclusions

Basic spectroscopic and fluorescence properties of ErP_5O_{14} monocrystals (in the monoclinic and orthorhombic forms) were measured. Due to high concentration quenching, ErP_5O_{14} monocrystals are not much promising as laser active media or infrared-to-visible up-convertors, at least under CW excitation and at room temperature. Nevertheless, further measurements of the lifetimes of the most interesting energy levels are required. We hope that pulse excitation will set on laser action in the 1.5–1.6 μm band, and also in the visible-via infrared-to-visible up-conversion.

Acknowledgements. We would like to thank Professor B. Hilczer and Dr. M. Polomska for the access to the Bruker Raman spectrograph, and for their help in performing the measurements. Absorption at liquid helium temperature was measured at the Institute for Low Temperature and Structure Research in Wroclaw. Thanks are also due to M.Sci. M. Balicki for computer calculations. This work was financially supported by the Committee for Scientific Research (KBN), grant No. 2P 302 02204.

Note added in proof: With the cooperation of Edinburgh Instruments, UK, and Dr. H. Malak at the Center for Fluoresence Spectroscopy, University of Baltimore, the lifetime of the fluorescence level $^4F_{3/2}$ was determined to be 380 ± 20 ns.

References

1. S.A. Pollack, D.B. Chang, N.L. Moise: J. Appl. Phys. **60**, 4077 (1986)
2. Y. Kimura, M. Nakazowa: J. Appl. Phys. **64**, 516 (1988)
3. L. Li, R. Moncorge, J.C. Sourian, C. Borel, Ch. Wyon: Opt. Commun. **107**, 61 (1994)
4. E. Lacot, F. Stoeckel, M. Chenevier: Phys. Rev. A **49**, 3997 (1994)
5. B. Pederson: Opt. Quantum Electron. **26**, 273 (1994)
6. R.J. Mears, S.R. Baker: Opt. Quantum Electron. **24**, 517 (1992)
7. L.F. Johnson, H.J. Gugenheim: Appl. Phys. Lett. **19**, 44 (1971)
8. A.J. Silversmith, W. Lenth, R.M. Macfarlane: Appl. Phys. Lett. **51**, 1977 (1987)
9. R. Micheletti, P. Minguzzi, M.A. Noginov, M. Tonelli: J. Opt. Soc. Am. B **11**, 2095 (1994)
10. M. Shojiya, M. Takahashi, R. Kanno: Appl. Phys. Lett. **65**, 1874 (1994)
11. F. Heine, E. Heumann, T. Danger, T. Schweizer, G. Huber: Appl. Phys. Lett. **65**, 383 (1994)
12. T. Danger, J. Koetke, R. Brede, E. Heumann, G. Huber: J. Appl. Phys. **76**, 1413 (1994)
13. D.L. Nicacio, E.A. Gouveia, A.M. Reis, N.M. Borges, A.S. Gruveia-Nieto: IEEE J. QE- **30**, 2634 (1994)
14. D. Piehler, D. Craven: *CLEO '94*, Anaheim (1994) Paper CMK4
15. R.A. McFarlane: Opt. Lett. **16**, 1397 (1991)
16. R.R. Stephens, R.A. McFarlane: Opt. Lett. **18**, 34 (1993)
17. H.P. Weber, T.C. Damen, H.G. Danielmeyer, B.C. Tofield: Appl. Phys. Lett. **22**, 534 (1973)
18. B.C. Tofield, H.P. Weber, T.C. Damen: Mater. Res. Bull. **9**, 435 (1974)
19. H.G. Danielmeyer, G. Huber, W.W. Krühler, J.P. Jeser: Appl. Phys. **2**, 335 (1973)
20. H.G. Danielmeyer, H.P. Weber: IEEE J. QE-**8**, 805 (1972)
21. W.W. Krühler, J.P. Jesser, H.G. Danielmeyer: Appl. Phys. **2**, 329 (1973)

22. S. Singh, D.C. Miller, J.R. Potopowicz, L.K.Schick: J. Appl. Phys. **46**, 1191 (1975)
23. F. Kaczmarek, M. Szymański: Appl. Phys. **13**, 55 (1977)
24. M. Szymański, J. Karolczak, F. Kaczmarek: Acta Phys. Polon. A **60**, 95 (1981)
25. B. Jeżowska-Trzebiatowska, Z. Mazurak, T. Lis: Acta Cryst. B **36**, 1639 (1980)
26. A. Katrusiak, F. Kaczmarek: Cryst. Res. Technol. **30**, 501 (1995)
27. F. Kaczmarek, M.B. Kosmina, A.B. Levin, B.P. Nazarenko, S.N. Kolpakov: J. Cryst. Growth **152**, 238 (1995)
28. V.L. Donlan, A.A. Santiago: J. Chem. Phys. **57**, 4717 (1972)
29. Z. Mazurak, W. Ryba-Romanowski, B. Jeżowska-Trzebiatowska: J. Lumin. **17**, 401 (1978)
30. L. Li, C. Wyon, R. Moncorge: IEEE J. QE- **28**, 1209 (1992)
31. W. Krupke, J.B. Gruber: J. Chem. Phys. **41**, 1225 (1964)
32. W. Krupke: Phys. Rev. **145**, 325 (1966)
33. W.T. Carnall, P.R. Fields, B.G. Wybourne: J. Chem. Phys. **42**, 3797 (1965)
34. K. Rajnisk: J. Chem. Phys. **43**, 847 (1965)
35. M.J. Weber: Phys. Rev. **157**, 262(1967); Phys. Rev. B **8**, 54 (1973)
36. D.E.C. Corbridge, E.J. Lowe: J. Chem. Soc. **1**, 493 (1954)
37. T. Miyakawa, D.L. Dexter: Phys. Rev. B **1**, 2961 (1970)
38. E.V. Zharikov, N.N. Il'ichev, S.P. Kalitin, V.V. Lapter, A.A. Malyutin, V.V. Osiko, P.P. Pasninin, A.M. Prokhorov, Z.S. Saidov, V.A. Smirnof, A.F. Umyskov, I.A. Scherbakov: Sov. J. Quantum Electron. **16**, 635 (1986)
39. R. Micheletti, P. Minguzzi, M.A. Noginov, M. Tonelli: J. Opt. Soc. Am. **11**, 2095 (1994)